Research Square

Preprints are preliminary reports that have not undergone peer review.
They should not be considered conclusive, used to inform clinical practice,
or referenced by the media as validated information.

Velocity-Obstacle and COLREGs-Based Safety Control for Underactuated USVs with a Fixed-Time Fuzzy Observer: Theory and Experiment

Zheng Wang

dlwz@dlmu.edu.cn

Dalian Maritime University

Yongsheng Zhao

Dalian Maritime University

Zhiyi Wang

Dalian Maritime University

Xiaohong Yan

Army Force Representative in Dalian

Dongdong Mu

Dalian Maritime University

Xiao Liang

Dalian Maritime University

Yiqi Wang

China Kunlun Contracting & Engineering Corporation Dalian Company

Qian Wang

CRRC DALIAN CO., LTD.

Article

Keywords: Fixed-Time, Fuzzy Observer, Velocity-Obstacle, Marine Experiment

Posted Date: October 22nd, 2026

DOI: https://doi.org/10.21203/rs.3.rs-11213717/v1

License: This work is licensed under a Creative Commons Attribution 4.0 International License.
Read Full License

Additional Declarations: No competing interests reported.

Velocity-Obstacle and COLREGs-Based Safety Control for Underactuated USVs with a Fixed-Time Fuzzy Observer: Theory and Experiments

Zheng Wang[1*], Yongsheng Zhao[1*], Zhiyi Wang[1], Xiaohong Yan[2], Dongdong Mu[1*], Xiao Liang[3], Yiqi Wang[4], Qian Wang[5]

[1]College of Marine Electrical Engineering, Dalian Maritime University, Dalian, 116026, China.
[2]Army Force Representative in Dalian, Dalian, 116083, Liaoning, China.
[3]Naval Architecture and Ocean Engineering College, Dalian Maritime University, Dalian, 116026, China.
[4]Instrumentation and Electrical Room, China Kunlun Contracting & Engineering Corporation Dalian Company, Dalian, 116023, Liaoning, China.
[5]Manufacturing Branch Comprehensive Room, CRRC DALIAN CO., LTD., Dalian, 116041, Liaoning, China.

*Corresponding author(s). E-mail(s): dlwz@dlmu.edu.cn; yszhao@dlmu.edu.cn; ddmu@dlmu.edu.cn;

Abstract

This paper addresses the safe waypoint-following problem of an underactuated unmanned surface vehicle (USV) operating in environments where moving obstacle vessels may appear along the planned route. First, to satisfy the International Regulations for Preventing Collisions at Sea (COLREGs), a collision-avoidance guidance strategy based on velocity-obstacle (VO) boundaries and COLREGs is proposed for three typical encounter scenarios: head-on, overtaking, and crossing.Different from optimization-oriented VO schemes that determine commands through searching or sampling in the admissible velocity region, the proposed method obtains the commanded heading directly from analytical VO boundary information, thereby ensuring collision avoidance while complying with COLREGs. Second, a fixed-time fuzzy observer is integrated into the USV control

framework to estimate external disturbances and lumped uncertainties encountered during navigation. A Lyapunov-based stability analysis is provided to prove that the closed-loop system achieves practical fixed-time stability. Finally, sea trials are performed on a 4.9-m USV platform, where virtual obstacle vessels are introduced to reproduce representative encounter scenarios. The obtained results confirm the effectiveness and engineering feasibility of the proposed collision-avoidance guidance method.

Keywords: Fixed-Time, Fuzzy Observer, Velocity-Obstacle, Marine Experiment

1 Introduction

Unmanned Surface Vehicles (USVs), as a type of marine unmanned platform with high autonomy, flexible deployment capability, and strong environmental adaptability, have been widely used in environmental monitoring, maritime patrol, and material supply missions [1][2]. Nevertheless, due to cost constraints and hull structural limitations, most USVs are configured as underactuated systems without lateral thrusters [3]. Moreover, in practical navigation scenarios, USVs are inevitably subjected to environmental disturbances caused by wind, waves, and currents, as well as the dynamic influence of surrounding obstacle vessels, which further complicates the theoretical analysis and engineering implementation of motion control.

Research on USV control mainly includes backstepping control [4], sliding mode control[5], model predictive control (MPC)[6], deep reinforcement learning [7], and fuzzy control [8]. Among these, fuzzy control is widely used in engineering owing to its strong robustness and simple implementation. For example, [9] developed an adaptive fuzzy control law for unconstrained nonlinear systems; [10] proposed a self-organizing fuzzy wavelet neural controller for model-free control; [11] employed fuzzy logic systems to approximate unknown nonlinearities in USV dynamics; [12] investigated observer-based fuzzy adaptive fault-tolerant control; and [13] designed a fuzzy state observer to estimate unmeasurable states.

Existing studies on USV collision avoidance and path planning can be broadly divided into optimization-based methods, deep reinforcement learning (DRL)-based methods, and dynamic window or artificial-potential-field-based methods.

For optimization-based methods, [14] combined barrier-certified techniques with model predictive control for multi-USV formation collision avoidance, while [15] achieved collision-free optimal planning by using constrained optimization and distributed MPC, respectively. For DRL-based methods, [16] proposed a COLREGs-compliant DQN-based collision-avoidance method by integrating maritime state representation, adaptive reward design, and an enhanced dueling double DQN architecture. [17] developed a multi-agent DRL approach for cooperative collision avoidance. Although these methods show good performance in simulations, their practical implementation remains difficult.[18] enhanced the DWA with fuzzy logic-based dynamic weight adjustment to achieve safer and smoother obstacle avoidance in complex dynamic environments.

For practical implementation, [19] proposed the velocity obstacle (VO) method, , which represents obstacles in the velocity space and provides an effective framework for collision avoidance. [20] developed a VO-based control barrier function, and [21] combined RVO with deep reinforcement learning for cooperative collision avoidance under limited information. Artificial potential field methods have also been widely used in path planning. [22] applied them to distributed guidance for collision avoidance and connectivity preservation, [23] introduced a rotational potential field to mitigate local minima and oscillation, and [24] combined them with a dynamic virtual vessel structure for intelligent guidance.

Most VO- and artificial-potential-field-based studies do not explicitly consider COLREGs. To address this, [25] unified path following and collision avoidance and designed guidance laws for head-on, overtaking, and crossing scenarios; [26] developed a COLREGs-compliant artificial potential field method; and [27] achieved dynamic collision avoidance under COLREGs using proactive velocity obstacles and motion prediction. However, existing studies mainly focus on general parametric trajectories, while collision avoidance under waypoint guidance remains insufficiently studied.

In terms of experimental validation of USV control methods, [28] verified an adaptive super-twisting controller for robust trajectory tracking through simulations and prototype sea trials. [29] demonstrated a resource-aware cooperative vector field with a self-triggered mechanism for synchronized path following in simulations and multi-vessel experiments. [30] validated an online sparse least-squares support vector machine for parameter identification and motion prediction using full-scale USV tests. [31] experimentally showed the potential of adaptive dynamic programming and deep reinforcement learning for USV control and path following. [32] further developed GVF-based collision-free target-tracking control methods and verified their effectiveness experimentally.

(1) Unlike the PVO method in [27], which relies on discrete-sampling-based optimization, the proposed VOBCG method derives continuous commands from analytical VO boundaries. This avoids the abrupt command changes and oscillations that may occur when command continuity is not explicitly considered, enabling smoother heading and surge-speed guidance and better engineering implementability.
(2) A fixed-time fuzzy observer (FT-FO)-based USV controller is developed, achieving faster disturbance-estimation convergence than the conventional fixed-time observer in [33]. Lyapunov analysis proves the practical fixed-time stability of the closed-loop system, while simulation verify its dynamic response and tracking accuracy in commanded-speed tracking.
(3) To validate the effectiveness of the proposed collision-avoidance control scheme, a marine USV experimental platform is established. For waypoint-tracking missions, waypoint routes are first planned on an electronic chart, and then a 4.9 m USV is deployed in open waters to perform waypoint-tracking tasks. By introducing virtual obstacle vessels, collision-avoidance maneuvers under three typical encounter scenarios, namely head-on, overtaking, and crossing, are simulated. The experimental results verify the feasibility, reliability, and engineering potential of the proposed collision-avoidance control strategy in real marine environments.

2 Problem Statement

2.1 USV Model

The planar motion of the considered underactuated USV is described by the following kinematic and dynamic equations:

$$\begin{cases} \dot{\eta} = R(\psi)\nu, \\ \dot{\nu} = \bar{f}(\nu) + M^{-1}\tau \end{cases} \tag{1}$$

where $\eta = [x, y, \psi]^T \in \mathbb{R}^3$ represents the surge-position coordinate, sway-position coordinate, and yaw angle of the USV in the earth-fixed frame, and $\nu = [u, v, r]^T \in \mathbb{R}^3$ denotes the velocity vector expressed in the body-fixed frame. The matrix $M \in \mathbb{R}^{3\times3}$ is the inertia matrix of the USV. The vector $\bar{f}(\nu) = [\bar{f}_u, \bar{f}_v, \bar{f}_r]^T \in \mathbb{R}^3$ is introduced to describe the normalized lumped dynamics, including model uncertainties and external disturbances. It is given by

$$\bar{f}(\nu) = M^{-1}\left(f(\nu) + \tau_d(t)\right), \tag{2}$$

where $f(\nu) = [f_u, f_v, f_r^i]^T \in \mathbb{R}^3$ denotes the uncertain nonlinear hydrodynamic term, and $\tau_d(t) = [\tau_{du}, \tau_{dv}, \tau_{dr}]^T \in \mathbb{R}^3$ represents the time-varying disturbance vector acting on the surge, sway, and yaw channels. Since the USV is underactuated, no direct control force is available in the sway direction. Therefore, the control input is written as $\tau = [\tau_u, 0, \tau_r]^T \in \mathbb{R}^3$, where τ_u and τ_r denote the surge force and yaw moment, respectively. The coordinate transformation matrix $R(\psi) \in \mathbb{R}^{3\times3}$ is defined as

$$R(\psi) = \begin{bmatrix} \cos\psi & -\sin\psi & 0 \\ \sin\psi & \cos\psi & 0 \\ 0 & 0 & 1 \end{bmatrix}. \tag{3}$$

2.2 Fuzzy-Logic Fundamentals

The fuzzy logic system (FLS) adopted in this work is constructed by a set of IF–THEN rules. Its N-th rule can be written as

$$\text{Rule}^{(N)}: \text{ If } x_1 \text{ is } A_1^N,\ x_2 \text{ is } A_2^N,\ \ldots,\ x_n \text{ is } A_n^N,\ \text{Then } y \text{ is } B^N. \tag{4}$$

In the above expression, N is the total number of fuzzy rules, $x = [x_1, x_2, \ldots, x_n] \in \mathbb{R}^n$ denotes the input vector of the FLS, and y is the corresponding output. For the q-th fuzzy rule, A_p^q denotes the fuzzy set associated with the p-th input variable, while B^q represents the corresponding fuzzy singleton, where $p = 1, 2, \ldots, n$ and $q = 1, 2, \ldots, N$.

By using the standard fuzzy basis-function representation, the output of the FLS can be rewritten in the following compact form:

$$y_B(x) = \xi^T \Phi(x) + \Omega, \tag{5}$$

where $\xi = [\xi^1, \ldots, \xi^N]^T$ denotes the adjustable fuzzy weight vector, $\Phi(x) = [\Phi^1(x), \Phi^2(x), \ldots, \Phi^N(x)]^T$ is the fuzzy basis-function vector, and Ω is the approximation error.

The normalized basis function corresponding to the q-th rule is given by

$$\Phi^q(x) = \frac{\prod_{p=1}^{n} \mu_{A_p^q}(x_p)}{\sum_{q=1}^{N} \prod_{p=1}^{n} \mu_{A_p^q}(x_p)}, \tag{6}$$

where $\mu_{A_p^q}(\cdot)$ denotes the membership function of the fuzzy set A_p^q.

2.3 Preliminaries

Assumption 1 *[1] In (2), the disturbance vector is specified as $\tau_d^i(t) = [\tau_{du}^i, \tau_{dv}^i, \tau_{dr}^i]^T$, where each component is time-varying but uniformly bounded, i.e. $\tau_{du}^i \le \bar{\tau}_{du}$, $\tau_{dv}^i \le \bar{\tau}_{dv}$, and $\tau_{dr}^i \le \bar{\tau}_{dr}$.*

Assumption 2 *[2] For any continuous function $f(x)$ on a compact domain Ξ and for any $\varepsilon > 0$, a fuzzy-logic approximator $y(x) = \xi^T \Phi(x)$ can be constructed such that*

$$\sup_{x \in \Xi} |f(x) - \xi^T \Phi(x)| \le \varepsilon. \tag{7}$$

Lemma 1 *[3] If there exists $\delta_1, \delta_2, \alpha, \theta \in (0,1), \beta \in (1, +\infty), \vartheta \in (0, +\infty)$, and consider LFC, $V(x(t))$ satisfying*

$$\dot{V}(x(t)) \le -\delta_1 V^{\alpha}(x(t)) - \delta_2 V^{\beta}(x(t)) + \vartheta \tag{8}$$

Then the system is practically fixed-time stable and the setting-time is expressed as

$$T \le T_{\max} := \frac{1}{\delta_1 \theta (1-\alpha)} + \frac{1}{\delta_2 \theta (\beta - 1)} \tag{9}$$

Lemma 2 *[34] For any vectors $a, b \in \mathbb{R}^n$, the following inequality holds:*

$$\boldsymbol{a}^{\mathrm{T}} \boldsymbol{b} \le c^p \frac{\|\boldsymbol{a}\|^p}{p} + c^{-q} \frac{\|\boldsymbol{b}\|^q}{q} \tag{10}$$

where the parameters satisfy $c > 0$, $p > 1$, $q > 1$, and $(p-1)(q-1) = 1$.

Lemma 3 *[35] Consider an estimate defined as $\hat{a} = -\tilde{a} + a^*$. For any positive real number $\rho > \frac{1}{2}$, the following inequality holds:*

$$\tilde{a}\hat{a} = -a^2 + aa^* \le \left(-a^2 + \frac{1}{2\rho} a^2 + \frac{\rho}{2} a^{*2} \right) \le \frac{-(2\rho - 1)}{2\rho} a^2 + \frac{\rho}{2} a^{*2} \tag{11}$$

which can be rewritten as:

$$\chi \tilde{a}\hat{a} + \frac{\chi(2\rho - 1)}{2\rho} a^2 \le \frac{\chi \rho}{2} a^{*2} \tag{12}$$

Lemma 4 *[1] Assume $x_1, x_2 \ge 0$, $0 < p \le 1$, and $q > 1$. Then the following inequalities hold:*

$$x_1^p + x_2^p \ge (x_1 + x_2)^p \tag{13}$$

$$x_1^q + x_2^q \ge 2^{1-q} (x_1 + x_2)^q \tag{14}$$

2.4 Control Objective

This paper further extends the single-USV trajectory tracking control framework proposed in [3] by incorporating obstacle avoidance into the control design. The control objective of this paper is stated as follows:

1. To enable the follower USV to approach the desired trajectory $\bar{P} = (\bar{x}, \bar{y})$ apidly and smoothly when it is far from the initial waypoint, ensuring smooth convergence without abrupt control output (the trajectory smoothing strategy for the waypoints follows previous study [2]).
2. To ensure that the position error $\xi_p == \sqrt{(x_d - x_F)^2 + (y_d - y_F)^2}$ and the yaw angle error $\xi_\psi = \psi_d - \psi$ converge within the constrained performance bounds, where x_F, y_F, ψ_F are follower USV states, x_d, y_d, ψ_d are defined in DVGS Design part.

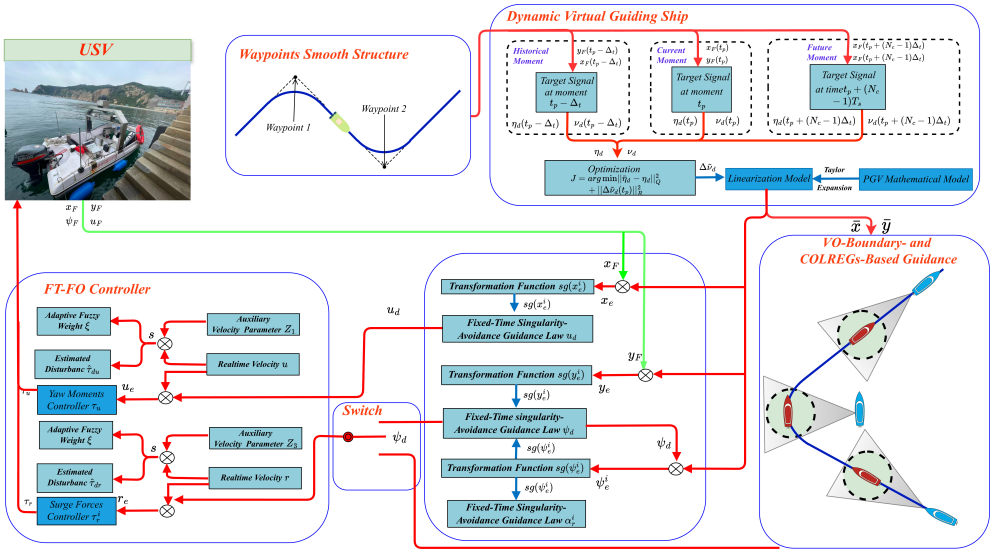


Fig. 1 Schematic diagram of the proposed control scheme.

3 VO-Boundary- and COLREGs-Based Guidance Method

During the execution of waypoint-based trajectory tracking tasks, USVs inevitably encounter other dynamically navigating vessels. To ensure navigational safety, it is necessary to perform appropriate collision avoidance maneuvers in accordance with the COLREGs. Focusing on typical encounter scenarios, including head-on, overtaking, and crossing situations, this paper develops a safety optimization mechanism that simultaneously accounts for trajectory tracking performance and navigational safety constraints. Furthermore, guidance and obstacle avoidance strategies are separately

designed depending on whether the target vessel enters the predefined ship safety domain.

Consider an own ship **os** and a target ship (obstacle) ts, whose equivalent radii are denoted by R_{os} and R_{ts}, respectively. The positions and velocities of the two vessels are represented by $p_{os} = (x_{os}, y_{os})$, $p_{ts} = (x_{ts}, y_{ts})$ and u_{os}, u_{ts}, respectively, and their geometric relationship is illustrated in Fig. 2.

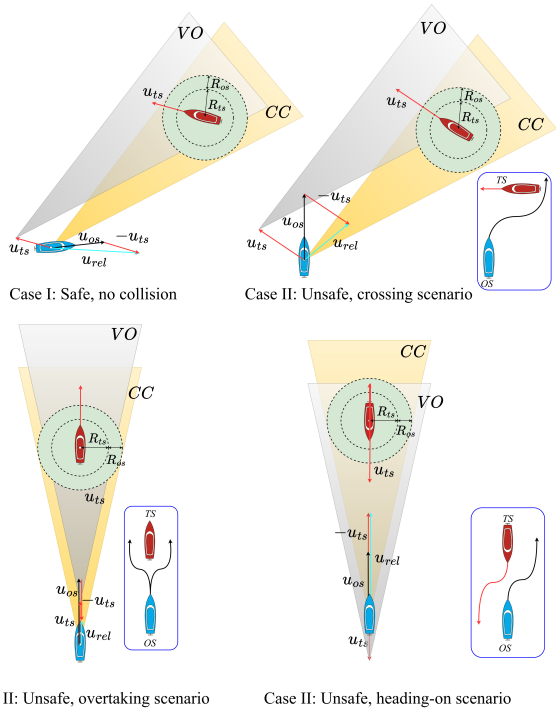


Fig. 2 VO conditions.

First, a unified description is established for the virtual reference motions of the own ship (OS) and the target ship (TS). The kinematic model of the virtual reference posture can be expressed as:

$$\begin{cases} \dot{x}_* = u_* \cos(\psi_*) \\ \dot{y}_* = u_* \sin(\psi_*) \end{cases} \tag{15}$$

where $* \in \{os, ts\}$, (x_*, y_*) denotes the planar position of the vessel, and u_* and ψ_* represent its surge speed and heading angle, respectively.

On this basis, according to the spatial relationship between the target ship and the own ship, the navigation process of the USV is classified into the following two scenarios.

Scenario 1 (Navigation outside the safety domain): When no target vessel enters the ship safety domain defined by the radius

$$d_{rel} \geq R_{os} + R_{ts} + R_{buf} \tag{16}$$

where $d_{rel} = ||P_{os} - p_{ts}||$, the current navigation environment is regarded as safe. In this case, the commanded heading of the own ship is directly determined by the desired heading ψ_d generated by the LOS guidance law, thereby enabling stable tracking of the predefined waypoint-based trajectory.

Scenario 2 (Obstacle avoidance navigation inside the safety domain): When a target vessel enters the ship safety domain

$$d_{rel} \leq R_{os} + R_{ts} + R_{buf} \tag{17}$$

the original LOS-based trajectory tracking guidance law is no longer sufficient to guarantee safe navigation of the USV. To mitigate potential collision risks, the guidance strategy is switched to a velocity obstacle (Velocity Obstacle, VO)-based obstacle avoidance control phase, in which the velocity of the own ship is constrained and adjusted in real time.

For the convenience of collision avoidance analysis, the own ship **os** is first mapped into the configuration space of the target ship ts by reducing the own ship to a point $P_{os} = (x_{os}, y_{os})$, and enlarging the geometric size of the target ship to a circular region with radius $R_{os}+R_{ts}$, which is denoted as $\hat{\text{ts}} = \left\{ p_{os} \in \mathbb{R}^2 \;\middle|\; \|p_{os} - p_{ts}\| \leq R_{os} + R_{ts} \right\}$.

On this basis, the collision cone (Collision Cone, CC) $\text{CC}_{os|ts}(u_{rel})$ is defined as the set of relative velocities between the point P_{os} and the enlarged obstacle $\hat{\text{ts}}$ that may result in a collision:

$$\text{CC}_{os|ts}(u_{rel}) = \left\{ u_{rel} \;\middle|\; \varrho(P_{os},\, u_{rel}) \cap \hat{\text{ts}} \neq \varnothing \right\} \tag{18}$$

as is illustrated in Fig. 2 yellow cone parts, where $\varrho(P_{os}, u_{rel})$ denotes a ray originating from P_{os} and extending in the direction of the relative velocity $u_{rel} = u_{os} - u_{ts}$.

From a geometric perspective, the collision cone $\text{CC}_{os|ts}$ can be described as a planar sector with its apex at P_{os}, formed by the two tangent lines from P_{os} to the enlarged obstacle $\hat{\text{ts}}$. Any relative velocity located within this sector will result in a future collision between the own ship **os** and the target ship ts. Conversely, if the relative velocity lies outside $\text{CC}_{os|ts}$, a collision can be avoided as long as both vessels maintain their current velocities.

It should be noted that the aforementioned collision cone $\text{CC}_{os|ts}(u_{rel})$ characterizes collision conditions in the relative velocity space. However, actual obstacle avoidance decisions require direct constraints on the absolute velocity of the own ship. Therefore, it is necessary to map the collision region from the relative velocity space into the absolute velocity space of the own ship.

The velocity obstacle generated by the target ship ts is represented by $\text{VO}_{os|ts}(u_{os})$. It describes the set of admissible own-ship velocities that would lead to a potential collision if both the own ship and the target ship continue to move with their current velocities. In other words, the collision-risk region in the absolute velocity space of the own ship can be obtained by shifting the relative-velocity collision cone $\text{CC}_{os|ts}(u_{rel})$ along the velocity vector of the target ship u_{ts}, as indicated by the gray cone region in Fig. 2. Accordingly, the velocity obstacle can be defined as

$$\text{VO}_{os|ts}(u_{os}) = \text{CC}_{os|ts}(u_{rel}) \oplus u_{ts} \tag{19}$$

Therefore, as long as the velocity of the own ship satisfie

$$\begin{aligned} u_{os}(t) &\notin \mathrm{VO}_{os|ts}(t) \\ u_{rel}(t) &\notin \mathrm{CC}_{os|ts}(t) \end{aligned} \tag{20}$$

a collision with the target ship ts can be avoided, as is illustrated in Fig. 2 Case I. When the target ship is stationary, its velocity obstacle set is geometrically equivalent to the corresponding collision cone, i.e., $u_{ts} = 0$.

Furthermore, to extend the collision cone $\mathrm{CC}_{os|ts}(u_{rel})$ and the velocity obstacle $\mathrm{VO}_{os|ts}(u_{os})$ to more general scenarios with varying velocities, as illustrated in Fig. 3, the half-aperture angle of the collision cone $\mathrm{CC}_{os|ts}(u_{rel})$ is defined as λ_{cc}.

$$\lambda_{cc} = \arcsin\left(\frac{R_{os} + R_{ts}}{d_{rel}}\right) \tag{21}$$

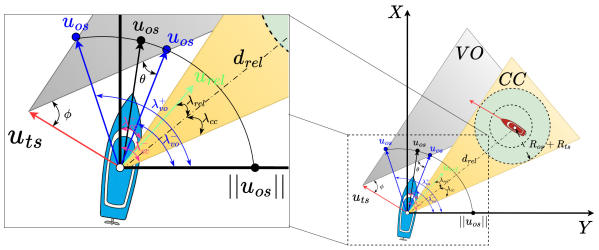


Fig. 3 angle conditions.

Define the relative position vector as $s_{rel} = p_{ts} - p_{os}$, and denote the angle between the relative velocity vector u_{rel} and the relative position vector s_{rel} as λ_{rel}, which is mathematically expressed as

$$\lambda_{rel} = \arccos\left(\frac{u_{rel}^T s_{rel}}{\|u_{rel}\|\|s_{rel}\|}\right) \tag{22}$$

It should be noted that when $\lambda_{rel} \geq \lambda_{cc}$, the relative velocity u_{rel} lies outside the collision cone $\mathrm{CC}_{os|ts}$, which is geometrically equivalent to the safety condition $u_{rel}(t) \notin \mathrm{CC}_{os|ts}(t)$ defined in (20). Conversely, if $\lambda_{rel} < \lambda_{cc}$, the own ship and the target ship are in a potential collision state. This angular criterion provides an intuitive and effective geometric measure for assessing collision risk between the vessels.

Based on the safety condition in absolute velocity space $u_{os}(t) \notin \mathrm{VO}_{os|ts}(t)$ defined in 20, and to ensure that the own ship's velocity always remains outside the velocity obstacle, the left and right directive avoidance angles, ψ^+_{VO} and ψ^-_{VO}, are further defined. Their geometric meaning is illustrated in Fig. 3. Specifically, $\psi^\pm_{VO}$ represents the heading angles corresponding to the intersections between the velocity circle—centered at the own ship position p_{os} with radius $|u_{os}|$—and the two boundaries of the velocity obstacle $\mathrm{VO}_{os|ts}$, which can be mathematically expressed as

$$\lambda^\pm_{VO} = \lambda^\pm_{\mathrm{CC}} + \theta^\pm, \theta^\pm = \arcsin\left(\frac{\|u_{ts}\|}{\|u_{os}\|\sin(\phi^\pm)}\right) \tag{23}$$

The boundary angles of the velocity obstacle $\mathrm{VO}_{os|ts}(t)$ are defined as $\lambda_{\mathrm{CC}}^{\pm} = \mathrm{atan2}(y_{ts} - y_{os},\, x_{ts} - x_{os}) + \lambda_{\mathrm{CC}}$, as illustrated in Fig. 3. The angles between the boundaries of $\mathrm{VO}_{os|ts}(t)$ and the lines connecting p_{os} to $s_{vo}^{\pm}$ are denoted by $\theta^{\pm}$. Here, the points $s_{vo}^{\pm}$ represent the intersections between a circle centered at p_{os} with radius $\|u_{os}\|$ and the two boundaries of $\mathrm{VO}_{os|ts}(t)$. Furthermore, the angles $\phi^{\pm}$ are defined as $\phi^{\pm} = \pi - \mathrm{atan2}(y_{ts} - y_{os},\, x_{ts} - x_{os}) + \lambda_{\mathrm{CC}}^{\pm}$.

According to COLREGs Rules 13, 14, and 15, the USV's avoidance maneuvers are classified into three navigation scenarios: head-on, overtaking, and crossing encounters, as illustrated in Fig. 4.

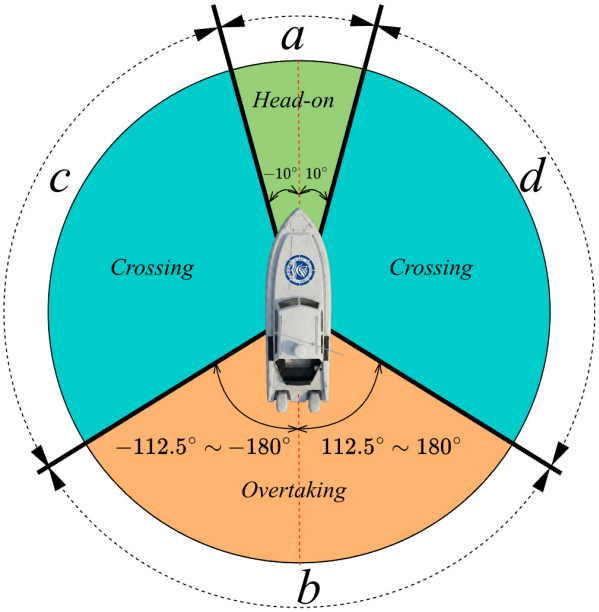


Fig. 4 domin conditions.

(1) For the crossing encounter between the own ship os and the target ship ts, COLREGs require the own ship to take a starboard-side avoidance action so as to prevent passing ahead of the target ship, as shown in Case II of Fig. 2. Accordingly, the desired heading command is chosen as

$$\psi_d = \lambda_{VO}^{-}. \tag{24}$$

(2) In the overtaking encounter, the own ship may avoid the target ship by turning either to starboard or to port, depending on their relative geometric relationship, as illustrated in Case III of Fig. 2. Therefore, the heading command is determined

according to the following switching rule:

$$\psi_d = \begin{cases} \lambda_{VO}^{-} & \text{if } \psi_{os} \geq \operatorname{atan2}(y_{ts} - y_{os}, x_{ts} - x_{os}) \\ \lambda_{VO}^{+} & \text{if } \psi_{os} < \operatorname{atan2}(y_{ts} - y_{os}, x_{ts} - x_{os}) \end{cases} \tag{25}$$

(3) When the own ship and the target ship are in a head-on encounter, in accordance with COLREGs Rule 14, the own ship should execute an avoidance maneuver to starboard, as illustrated in Case V of Fig. 2. The selection of the commanded heading follows the same rule as defined in Eq. (24).

3.1 Fixed-Time Fuzzy-Observer-Based Controller Design

To improve the disturbance-rejection capability of the closed-loop system under uncertain marine environments, the fuzzy approximation technique is combined with fixed-time stability theory to estimate unknown nonlinear disturbance terms. On this basis, a fixed-time adaptive fuzzy disturbance observer is constructed for online reconstruction of the external disturbances. Let Z be an auxiliary velocity-observation variable, and define the observation error as $s = v - Z$, where $Z = [Z_1, Z_2, Z_3]^{\mathrm{T}}$. Then, the proposed adaptive fixed-time fuzzy disturbance observer is formulated as follows.

$$\begin{cases} \dot{Z} = \dfrac{1}{M_0}(-C_0 v - D_0 v) + \dfrac{1}{M_0}\tau + \hat{\xi}^T \Phi(v) + a(v - Z)^m + b(v - Z)^n \\ \dot{\hat{\xi}} = \mu_1(\Phi(\nu)s^T - \mu_2 \hat{\xi}) \end{cases} \tag{26}$$

where τ_d denotes the vector of external disturbances in (2), and $s = [s_u, s_v, s_r]^{\mathrm{T}}$ represents the observation error vector. The design parameters are selected to satisfy the following requirements: $a, b \in \mathbb{R}^{3\times 3}$ are symmetric positive definite diagonal matrices, the fractional-order exponents are chosen such that $0 < m < 1$ and $n > 1$, and $\mu_1, \mu_2 > 0$ are adaptive gain parameters.

According to the definition of fuzzy approximation function (5), the true disturbance τ_d can be represented by the ideal fuzzy system together with a bounded approximation error, while its online estimate is generated using adaptive weights $\dot{\hat{\xi}}$. Specifically, the true disturbance τ_d, the estimated disturbance based on the ideal weights $\hat{\tau}_d(\boldsymbol{v} \mid \boldsymbol{W}^*)$, and the estimated disturbance based on the adaptive weights $\hat{\tau}_d(\boldsymbol{v} \mid \hat{\boldsymbol{W}})$ are respectively expressed as

$$\begin{aligned} \tau_d(v) &= \hat{\tau}_d(v \mid W^*) + \Omega = \xi^{*T} \Phi(v) + \Omega \\ \hat{\tau}_d(v \mid \hat{W}) &= \hat{\xi}^T \Phi(v) \end{aligned} \tag{27}$$

where $W^{*\mathrm{T}} = [W_u^{*\mathrm{T}}, W_v^{*\mathrm{T}}, W_r^{*\mathrm{T}}]^{\mathrm{T}}$ denotes the ideal weight matrix, $\hat{W}^{\mathrm{T}} = [\hat{W}_u^{\mathrm{T}}, \hat{W}_v^{\mathrm{T}}, \hat{W}_r^{\mathrm{T}}]^{\mathrm{T}}$ represents the adaptive weight matrix, and $\xi^{*\mathrm{T}} = [\xi_u^{*\mathrm{T}}, \xi_v^{*\mathrm{T}}, \xi_r^{*\mathrm{T}}]^{\mathrm{T}}$ denotes the corresponding ideal weight vector. The term Ω denotes the fuzzy approximation error. The weight estimation error is defined as $\tilde{W} = W^* - \hat{W}$. By substituting $\hat{\tau}_d(\boldsymbol{v} \mid W^*)$ and $\hat{\tau}_d(\boldsymbol{v} \mid \hat{W})$ into the disturbance representation and further substituting

the resulting expressions into the observation error dynamics, the time derivative of the observation error s can be obtained.

$$\begin{aligned}\dot{s} &= \hat{\tau}_d(\boldsymbol{v} \mid \boldsymbol{W}^*) + \Omega - \hat{\tau}_d(\boldsymbol{v} \mid \hat{\boldsymbol{W}}) - \boldsymbol{a}\boldsymbol{s}^m - \boldsymbol{b}\boldsymbol{s}^n \\ &= \tilde{\xi}^T \Phi(x) + \Omega - \boldsymbol{a}\boldsymbol{s}^m - \boldsymbol{b}\boldsymbol{s}^n\end{aligned} \tag{28}$$

To realize the simultaneous regulation of yaw dynamics and surge motion, the tracking errors are introduced as follows: $r_e = r - r_d$ for the yaw rate, $\psi_e = \psi - \psi_d$ for the yaw angle, and $u_e = u - u_d$ for the surge velocity. Here, r_d denotes the desired yaw rate, which is generated by

$$r_d = -k_{\varphi 1} \operatorname{sig}^p(\psi_e) - k_{\varphi 2} \operatorname{sig}^q(\psi_e) + \dot{\psi}_d \tag{29}$$

Furthermore, by differentiating the tracking errors u_e and r_e and combining them with the vessel dynamic model (1), the following error dynamics can be obtained:

$$\begin{aligned}\dot{u}_e &= \dot{u} - \dot{u}_d = F_u + \tau_{du} + m_{11}^{-1}\tau_u - \dot{u}_d \\ \dot{r}_e &= \dot{r} - \dot{r}_d = F_r + \tau_{dr} + m_{33}^{-1}\tau_r - \dot{r}_d\end{aligned} \tag{30}$$

Based on (30), the control laws for the yaw rate and surge velocity are designed as follows:

$$\begin{aligned}\tau_u &= m_{11}\left(-k_{u1} \operatorname{sig}^m(u_e) - k_{u2} \operatorname{sig}^n(u_e) - F_u - \hat{\tau}_{du} + \dot{u}_d\right) \\ \tau_r &= m_{33}\left(-k_{r1} \operatorname{sig}^m(r_e) - k_{r2} \operatorname{sig}^n(r_e) - F_r - \hat{\tau}_{dr} + \dot{r}_d\right)\end{aligned} \tag{31}$$

Here, $0 < p < 1$ and $q > 1$, and the control gains k_{u1}, k_{u2}, k_{r1}, $k_{r2} \in \mathbb{R}^+$ are to be designed. The stability analysis is conducted as follows. Select the positive-definite Lyapunov functionV_2

$$V_2 = \frac{1}{2}u_e^2 + \frac{1}{2}r_e^2 + \frac{1}{2}s^{\mathrm{T}}s + \frac{1}{2\mu_1}\tilde{\xi}^{\mathrm{T}}\tilde{\xi} \tag{32}$$

By differentiating (32) and substituting the error dynamics $\dot{s}$ and the adaptive parameter $\dot{\xi}$ into $\dot{V}_2$, we obtain:

$$
\begin{aligned}
\dot{V}_2 = & -k_{u1}(u_e^2)^{\frac{m+1}{2}} - k_{u2}(u_e^2)^{\frac{n+1}{2}} - k_{r1}(r_e^2)^{\frac{m+1}{2}} - k_{r2}(r_e^2)^{\frac{n+1}{2}} \\
& + u_e\tilde{\tau}_{du} + r_e\tilde{\tau}_{dr} \\
& - \lambda_{\min}(\boldsymbol{a})(\boldsymbol{s}^{\mathrm{T}}\boldsymbol{s})^{\frac{m+1}{2}} - \lambda_{\min}(\boldsymbol{b})(\boldsymbol{s}^{\mathrm{T}}\boldsymbol{s})^{\frac{n+1}{2}} \\
& + \boldsymbol{s}^{\mathrm{T}}\Omega + \boldsymbol{s}^{\mathrm{T}}\Phi(\nu)\tilde{\xi}^{\mathrm{T}} - \frac{1}{\mu_1}\tilde{\xi}^{\mathrm{T}}\dot{\hat{\xi}} \\
= & -k_{u1}(u_e^2)^{\frac{m+1}{2}} - k_{u2}(u_e^2)^{\frac{n+1}{2}} - k_{r1}(r_e^2)^{\frac{m+1}{2}} - k_{r2}(r_e^2)^{\frac{n+1}{2}} \\
& - \lambda_{\min}(\boldsymbol{a})(\boldsymbol{s}^{\mathrm{T}}\boldsymbol{s})^{\frac{m+1}{2}} - \lambda_{\min}(\boldsymbol{b})(\boldsymbol{s}^{\mathrm{T}}\boldsymbol{s})^{\frac{n+1}{2}} \\
& + \tilde{\xi}^{\mathrm{T}}\left(\Phi(\nu)\boldsymbol{s}^{\mathrm{T}} - \frac{1}{\mu_1}\dot{\hat{\xi}}\right) \\
& + \boldsymbol{s}^{\mathrm{T}}\Omega + u_e\tilde{\tau}_{du} + r_e\tilde{\tau}_{dr} \\
= & -k_{u1}(u_e^2)^{\frac{m+1}{2}} - k_{u2}(u_e^2)^{\frac{n+1}{2}} - k_{r1}(r_e^2)^{\frac{m+1}{2}} - k_{r2}(r_e^2)^{\frac{n+1}{2}} \\
& - \lambda_{\min}(\boldsymbol{a})(\boldsymbol{s}^{\mathrm{T}}\boldsymbol{s})^{\frac{m+1}{2}} - \lambda_{\min}(\boldsymbol{b})(\boldsymbol{s}^{\mathrm{T}}\boldsymbol{s})^{\frac{n+1}{2}} \\
& + \boldsymbol{s}^{\mathrm{T}}\Omega + \mu_2\tilde{\xi}^{\mathrm{T}}\hat{\xi} + u_e\tilde{\tau}_{du} + r_e\tilde{\tau}_{dr}
\end{aligned}
\tag{33}
$$

According to Lemma 2, the following inequality can be established for the disturbance approximation error term:

$$
s^{\mathrm{T}}\Omega \leq \frac{\varsigma_0^{m+1}}{m+1}\|s\|^{m+1} + \frac{\varsigma_0^{-\left(\frac{1}{m}+1\right)}}{\frac{1}{m}+1}\|\Omega^*\|^{\frac{1}{m}+1} \tag{34}
$$

Here, $\mathcal{S}_0 \in \mathbb{R}^+$, and applying Young's inequality, the disturbance-related terms can be scaled and bounded as follows:

$$
\begin{aligned}
r_e\tilde{\tau}_{dr} &\leq \frac{1}{2}r_e^2 + \frac{1}{2}\tilde{\tau}_{dr}^2 \\
u_e\tilde{\tau}_{du} &\leq \frac{1}{2}u_e^2 + \frac{1}{2}\tilde{\tau}_{du}^2
\end{aligned}
\tag{35}
$$

Substituting the above inequalities into (33) and rearranging yields:

$$
\begin{aligned}
\dot{V}_2 \leq & -k_{u1}(u_e^2)^{\frac{m+1}{2}} - k_{u2}(u_e^2)^{\frac{n+1}{2}} - k_{r1}(r_e^2)^{\frac{m+1}{2}} - k_{r2}(r_e^2)^{\frac{n+1}{2}} \\
& - \left(\lambda_{\min}(\boldsymbol{a}) - \frac{\varsigma_0^{m+1}}{m+1}\right)\|s\|^{m+1} - \lambda_{\min}(\boldsymbol{b})\|s\|^{n+1} \\
& + \frac{\varsigma_0^{-\left(\frac{1}{m}+1\right)}}{\frac{1}{m}+1}\|\Omega^*\|_m^{\frac{1}{m}+1} + \mu_2\tilde{\xi}^{\mathrm{T}}\hat{\xi} + \frac{1}{2}r_e^2 + \frac{1}{2}\tilde{\tau}_{dr}^2 + \frac{1}{2}u_e^2 + \frac{1}{2}\tilde{\tau}_{du}^2
\end{aligned}
\tag{36}
$$

Here, Ω^* denotes the maximum of Ω, and $\lambda_{\min}(\cdot)$ represents the minimum eigenvalue of a matrix. Further, based on lemma (4), we obtain:

$$
\begin{aligned}
\mu_2\tilde{\xi}^{\mathrm{T}}\hat{\xi} &= \mu_2\left(\tilde{\xi}^{\mathrm{T}}\xi^* - \tilde{\xi}^{\mathrm{T}}\tilde{\xi}\right) \\
&\leq \mu_2\left(\|\tilde{\xi}\|\|\xi^*\| - \|\tilde{\xi}\|^2\right) \\
&\leq \mu_2\left(-\|\tilde{\xi}\|^2 + \frac{1}{2\varphi}\|\tilde{\xi}\|^2 + \frac{\varphi}{2}\|\xi^*\|^2\right) \\
&= -\frac{\mu_2(2\varphi-1)}{2\varphi}\|\tilde{\xi}\|^2 + \frac{\mu_2\varphi}{2}\|\xi^*\|^2
\end{aligned} \tag{37}
$$

Further scaling and rearranging (36) yields:

$$
\begin{aligned}
\dot{V}_2 \leq\ & -k_{u1}(u_e^2)^{\frac{m+1}{2}} - k_{u2}(u_e^2)^{\frac{n+1}{2}} - k_{r1}(r_e^2)^{\frac{m+1}{2}} - k_{r2}(r_e^2)^{\frac{n+1}{2}} \\
& - \left(\lambda_{\min}(\boldsymbol{a}) - \frac{\varsigma_0^{m+1}}{m+1}\right)\|\boldsymbol{s}\|^{m+1} - \lambda_{\min}(\boldsymbol{b})\|\boldsymbol{s}\|^{n+1} + \frac{\varsigma_0^{-\left(\frac{1}{m}+1\right)}}{\frac{1}{m}+1}\|\Omega^*\|_m^{\frac{1}{m}+1} \\
& - \left(\frac{\mu_2(2\varphi-1)}{4\varphi}\|\tilde{\xi}\|^2\right)^{\frac{m+1}{2}} + \left(\frac{\mu_2(2\varphi-1)}{4\varphi}\|\tilde{\xi}\|^2\right)^{\frac{m+1}{2}} + \frac{\mu_2}{2}\tilde{\xi}^{\mathrm{T}}\hat{\xi} \\
& - \left(\frac{\mu_2(2\varphi-1)}{4\varphi}\|\tilde{\xi}\|^2\right)^{\frac{n+1}{2}} + \left(\frac{\mu_2(2\varphi-1)}{4\varphi}\|\tilde{\xi}\|^2\right)^{\frac{n+1}{2}} + \frac{\mu_2}{2}\tilde{\xi}^{\mathrm{T}}\hat{\xi}
\end{aligned} \tag{38}
$$

$$
\begin{aligned}
\dot{V}_2 \leq\ & -\hbar_1\left[\left(\frac{1}{2}u_e^2\right)^{\frac{m+1}{2}} + \left(\frac{1}{2}r_e^2\right)^{\frac{m+1}{2}} + \left(\frac{1}{2}\|\boldsymbol{s}\|^2\right)^{\frac{m+1}{2}} + \left(\frac{1}{2\mu_1}\|\tilde{\xi}\|^2\right)^{\frac{m+1}{2}}\right] \\
& - \hbar_2\left[\left(\frac{1}{2}u_e^2\right)^{\frac{n+1}{2}} + \left(\frac{1}{2}r_e^2\right)^{\frac{n+1}{2}} + \left(\frac{1}{2}\|\boldsymbol{s}\|^2\right)^{\frac{n+1}{2}} + \left(\frac{1}{2\mu_1}\|\tilde{\xi}\|^2\right)^{\frac{n+1}{2}}\right] \\
& + \left(\frac{\mu_2(2\varphi-1)}{4\varphi}\|\tilde{\xi}\|^2\right)^{\frac{m+1}{2}} + \left(\frac{\mu_2(2\varphi-1)}{4\varphi}\|\tilde{\xi}\|^2\right)^{\frac{n+1}{2}} + \mu_2\tilde{\xi}^{\mathrm{T}}\hat{\xi} \\
& + \frac{\varsigma_0^{-(\frac{1}{m}+1)}}{\frac{1}{m}+1}\|\Omega^*\|_m^{\frac{1}{m}+1} + \frac{1}{2}r_e^2 + \frac{1}{2}\tilde{\tau}_{du}^2 + \frac{1}{2}u_e^2 + \frac{1}{2}\tilde{\tau}_{dr}^2
\end{aligned} \tag{39}
$$

By appropriately selecting the parameters such that $\frac{\mu_2(2\varphi-1)}{4\varphi}\left\|\tilde{\xi}\right\|^2 \leq 1$, and according to Lemma 3, the following inequalities hold:

$$
\begin{aligned}
&\left(\frac{\mu_2(2\varphi-1)}{4\varphi}\|\tilde{\xi}\|^2\right)^{\frac{m+1}{2}}+\frac{\mu_2\tilde{\xi}^{\mathrm{T}}\hat{\xi}}{2}\\
&\leq \frac{\mu_2(2\varphi-1)}{4\varphi}\|\tilde{\xi}\|^2+\vartheta_0+\frac{\mu_2\tilde{\xi}^{\mathrm{T}}\hat{\xi}}{2}\\
&\leq \frac{\mu_2(2\varphi-1)}{4\varphi}\|\tilde{\xi}\|^2-\frac{\mu_2(2\varphi-1)}{4\varphi}\|\tilde{\xi}\|^2+\frac{\mu_2\varphi}{4}\|\xi^*\|^2+\vartheta_0\\
&\leq \frac{\mu_2\varphi}{4}\|\xi^*\|^2+\vartheta_0
\end{aligned}
\tag{40}
$$

$$
\begin{aligned}
&\left(\frac{\mu_2(2\varphi-1)}{4\varphi}\|\tilde{\xi}\|^2\right)^{\frac{n+1}{2}}+\frac{\mu_2\tilde{\xi}^{\mathrm{T}}\hat{\xi}}{2}\\
&\leq \frac{\mu_2(2\varphi-1)}{4\varphi}\|\tilde{\xi}\|^2+\frac{\mu_2\tilde{\xi}^{\mathrm{T}}\hat{\xi}}{2}\\
&\leq \frac{\mu_2\varphi}{4}\|\xi^*\|^2
\end{aligned}
$$

Here, ϑ_0 denotes a small positive constant. Substituting (40) into (39) and further simplifying yields:

$$
\begin{aligned}
\dot{V}_2 &\leq -\hbar_1 V_2^{\frac{m+1}{2}}-2^{\frac{1-n}{2}}\hbar_2 V_2^{\frac{n+1}{2}}\\
&\quad+\frac{\mu_2\varphi}{2}\|W^*\|^2+\frac{\varsigma_0^{-(\frac{1}{m}+1)}}{\frac{1}{m}+1}\|\Omega^*\|_m^{\frac{1}{m}+1}+\frac{1}{2}r_e^2+\frac{1}{2}\tilde{\tau}_{dr}^2+\frac{1}{2}u_e^2+\frac{1}{2}\tilde{\tau}_{du}^2\\
&=-\hbar_1 V_2^{\frac{m+1}{2}}-2^{\frac{1-n}{2}}\hbar_2 V_2^{\frac{n+1}{2}}+\vartheta_1
\end{aligned}
\tag{41}
$$

In the above expression,

$$
\vartheta_1=\vartheta_0+\frac{\mu_2\varphi}{2}\|\xi^*\|_F^2+\frac{\varsigma_0^{-(\frac{1}{m}+1)}}{\frac{1}{m}+1}\|\Omega^*\|_m^{\frac{1}{m}+1}+\frac{1}{2}r_e^2+\frac{1}{2}\tilde{\tau}_{dr}^2+\frac{1}{2}u_e^2+\frac{1}{2}\tilde{\tau}_{du}^2
\tag{42}
$$

According to (41), the Lyapunov function V_2 satisfies:

$$
\lim_{t\to\infty}V_2(t)\leq\min\left\{\left(\frac{\vartheta_1}{\hbar_1}\right)^{\frac{2}{m+1}},\left(\frac{2^{\frac{2}{1-n}}\vartheta_1}{\hbar_2}\right)^{\frac{2}{n+1}}\right\}
\tag{43}
$$

According to lemma 1, $\dot{V}_2$ exhibits actual fixed-time convergence, indicating that the disturbance observation error is bounded and converges within a fixed time. Consequently, the convergence time of the fixed-time observer satisfies

$$
T_1\leq\frac{1}{\hbar_1\theta(1-\frac{m+1}{2})}+\frac{1}{2^{\frac{1-n}{2}}\hbar_2\theta(\frac{n+1}{2}-1)}
$$

where $0<\theta<1$.

4 Numerical Simulation and Field Experiment Results

In this section, the "Lanxin" USV is adopted as the mathematical model [3], and a Simulink-based simulation platform is established to validate the effectiveness of the proposed COLREGs-constrained velocity-obstacle-based safe navigation control scheme incorporating a fixed-time fuzzy disturbance observer. The detailed USV dynamics and the mathematical formulation of the external disturbance $\tau_d(t)$ can be found in [1]. The parameters of the proposed control strategy are summarized in Table 1. The initial state of the USV is set as $x = 52$, $y = 82$, and $\psi = -\pi/2$. The navigation task is to track a set of discontinuous waypoints defined by $\bar{x} = [180, 380, 380, 180, 180]$ and $\bar{y} = [170, 170, 370, 370, 170]$. To ensure trajectory smoothness, the waypoint smoothing strategy described in [2] is employed. Along the reference route, four moving target ships (TSs) are introduced to generate encounter, overtaking, and crossing scenarios consistent with those described in Fig 2. The motion of each TS is defined as

$$\boldsymbol{P}_{ts}^{n}(t) = \begin{bmatrix} x_{ts}^{n}(t) \\ y_{ts}^{n}(t) \end{bmatrix} = \begin{bmatrix} x_{\text{init}}^{n} \\ y_{\text{init}}^{n} \end{bmatrix} + \begin{bmatrix} v_{\text{obs},x}^{n} \\ v_{\text{obs},y}^{n} \end{bmatrix} (t - t_{\text{start}}^{n}), \quad t_{\text{start}}^{n} \leq t \leq t_{\text{end}}^{n}, \tag{44}$$

where $n = 1, \ldots, 4$ denotes the index of the target ship. Specifically, the initial positions, velocities, and motion starting times of the four TSs are given as $(x_{\text{init}}^{1}, y_{\text{init}}^{1}) = (390, 240)$, $(v_{\text{obs},x}^{1}, v_{\text{obs},y}^{1}) = (-1, -1)$, $t_{\text{start}}^{1} = 0$; $(x_{\text{init}}^{2}, y_{\text{init}}^{2}) = (330, 282)$, $(v_{\text{obs},x}^{2}, v_{\text{obs},y}^{2}) = (1, 0)$, $t_{\text{start}}^{2} = 100$; $(x_{\text{init}}^{3}, y_{\text{init}}^{3}) = (235, 370)$, $(v_{\text{obs},x}^{3}, v_{\text{obs},y}^{3}) = (1, 0)$, $t_{\text{start}}^{3} = 200$; and $(x_{\text{init}}^{4}, y_{\text{init}}^{4}) = (180, 310)$, $(v_{\text{obs},x}^{4}, v_{\text{obs},y}^{4}) = (0, -0.4)$, $t_{\text{start}}^{4} = 240$, respectively.

Table 1 Control Parameters.

Methods	Parameters
VOBCG	$R_{os} = 10$,$R_{ts} = 5$,$R_{buf} = 5$,
FT-FOC	$\mu_1 = 0.4, \mu_2 = 2, m = 0.6, n = 1.5, p = 0.8, q = 1.2$, $k_{\psi 1} = 0.1$, $k_{\psi 2} = 0.2$,$k_{u1} = 6.5$, $k_{u2} = 3$,$k_{r1} = 10$, $k_{r2} = 6$

Compared to the Proactive Velocity Obstacle (PVO) method proposed in [27], the VOBCG method presented in this paper significantly addresses the oscillation issues in control outputs, achieving smooth and stable commands for both yaw angle and surge velocity. As illustrated in Fig. 5.a, when encountering a typical crossing scenario with a Target Ship (TS) approaching from the starboard side, the CVO method demonstrates superior trajectory tracking precision and maintains a closer adherence to the reference path. Further analysis of Fig. 5.b and Fig. 5.c reveals that the control command curves generated by CVO exhibit high continuity and smoothness. This effectively eliminates the discrete chattering phenomena inherent in the PVO method, better aligning with the physical constraints of actual ship propulsion systems.

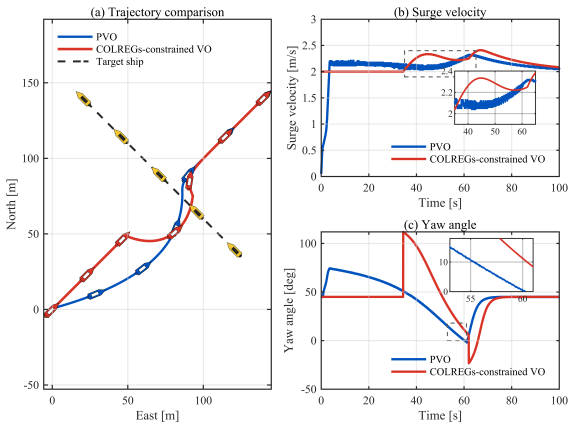


Fig. 5 Performance comparison and analysis between the proposed COLREGs-constrained VO method and the PVO method.

The simulation trajectories of the USV performing waypoint tracking tasks while adhering to COLREGs collision avoidance rules are illustrated in Fig. 6. To comprehensively validate the effectiveness of the proposed algorithm under various typical encounter scenarios, four representative dynamic Target Ships (TS1–TS4) were designed. Specifically, TS1 and TS2 simulate crossing scenarios where obstacles approach from the USV's starboard side; TS3 represents a head-on encounter; and TS4 is utilized to verify the overtaking maneuver.

Detailed local magnified views of each obstacle avoidance process are presented in Fig. 7. **Crossing Scenarios (Fig. 7.a & b)**: When confronted with threats from TS1 and TS2 on the starboard side, the USV strictly adheres to COLREGs by executing a starboard turn to ensure passing behind the stern of the target ship. **Head-on Scenario (Fig. 7.c)**: During the encounter with TS3, the USV proactively steers to starboard, ensuring a safe "port-to-port" passage for both vessels. **Overtaking Scenario (Fig. 7.d)**: Facing the slower-moving TS4 sailing in the same direction, the USV completes the avoidance maneuver and successfully overtakes the target through a starboard turn. The aforementioned simulation results demonstrate that the proposed avoidance strategy effectively guides the USV to make collision avoidance decisions that are both rule-compliant and physically feasible in complex dynamic navigation environments.

Figure 8 illustrates the evolution of position errors between the own ship (OS) position $P = (x, y)$ and the smooth reference trajectory $P_s = (x_s, y_s)$, including the component errors (in x and y directions) and the absolute position error $P_{err}^s = \sqrt{(x - x_s)^2 + (y - y_s)^2}$. The gray shaded areas in the figure indicate the time intervals during which the OS is executing obstacle avoidance maneuvers. Experimental results demonstrate that although the position error increases during the avoidance maneuvers, the USV is capable of smoothly and rapidly re-tracking the reference trajectory once clear of the obstacle threats, leveraging the convergence performance of its controller.

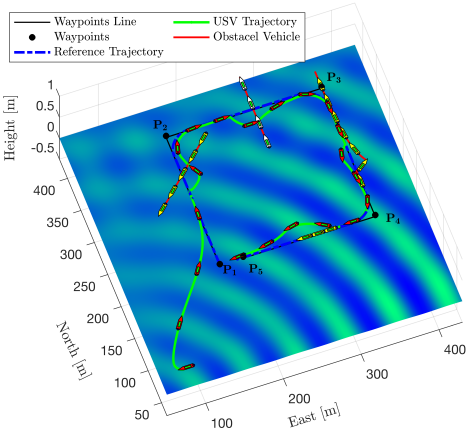


Fig. 6 Trajectory tracking and obstacle avoidance results of the USV for a smooth reference trajectory composed of waypoints P_1–P_5 in the presence of multiple dynamic obstacles (TS1–TS4).

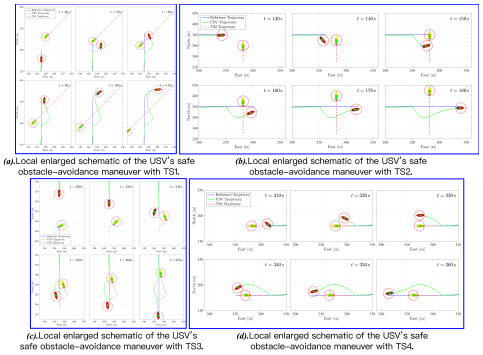


Fig. 7 Locally magnified views of the obstacle avoidance process under different encounter situations, including overtaking, head-on, and crossing scenarios.

Figure 9 presents the relative distance curves between the OS and the virtual target ships TS1–TS4 over time. To ensure navigational safety, a safety distance threshold of 20 m is established in the system (represented by the red dashed line in the figure). It can be observed that throughout the entire obstacle avoidance process, the minimum relative distance between the OS and all obstacles remains strictly above 20 m. This fully validates the safety and effectiveness of the proposed avoidance strategy in complex dynamic environments.

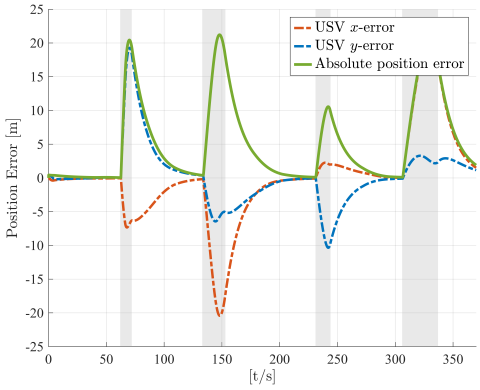


Fig. 8 Evolution of position tracking errors between the USV and the reference trajectory P_s under obstacle avoidance maneuvers.

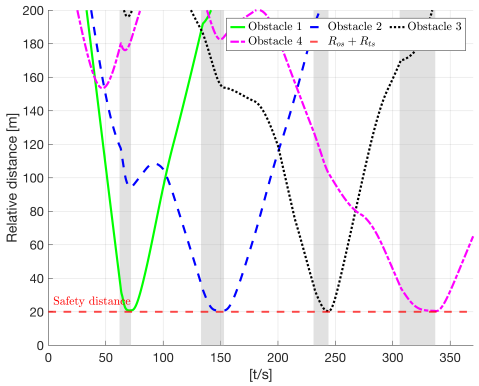


Fig. 9 Relative distance curves between the USV and virtual obstacles TS1–TS4.

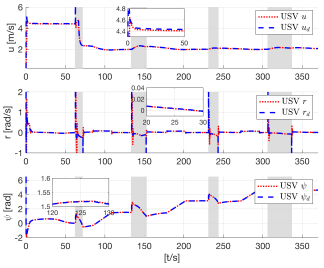


Fig. 10 Tracking performance curves of surge velocity u, yaw angle ψ, and yaw rate r relative to their respective reference signals.

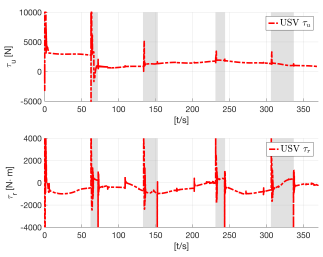


Fig. 11 Controller output curves τ_u and τ_r under obstacle avoidance maneuvers.

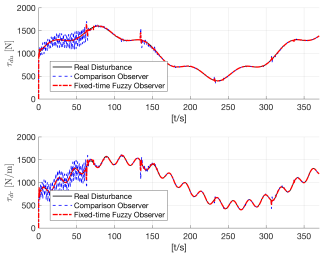


Fig. 12 Comparison of the proposed fixed-time fuzzy disturbance observer with the Fixed time disturbance observer.

Fig. 10 illustrates the tracking performance of the unmanned surface vehicle (USV) under the proposed controller. The reference commands are generated by LOS guidance in [2], including the reference surge velocity u_d, reference heading angle ψ_d, and reference yaw rate r_d. It can be seen from the simulation results that the proposed controller enables the USV to follow these time-varying reference commands with fast response and high tracking accuracy, which further confirms the stability and effectiveness of the closed-loop control system.

Fig. 11 depicts the controller outputs, namely the surge force τ_u and yaw moment τ_r. It can be observed that during obstacle avoidance maneuvers and trajectory tracking, the control inputs remain within the physical constraints of the actuators and exhibit favorable dynamic response characteristics at maneuver switching instants.

The observer-estimation results are presented in Fig. 12, where the proposed fixed-time fuzzy disturbance observer is compared with the fixed-time observer reported in [33]. It is observed that the proposed design can reconstruct the disturbance more rapidly and reduce the estimation error more effectively when external disturbances are present.

4.1 Field Experiment Results

Open-water experiments were performed to further validate the effectiveness and practical deployability of the proposed control scheme in real marine environments. A 4.9 m USV was used as the experimental platform. The architecture of the field-test system is presented in Fig. 13. It consists of a shore-based station and an onboard execution module. The shore-based station is used for electronic chart display and real-time visual monitoring, whereas the onboard module is responsible for algorithm execution on a compact industrial computer equipped with the Kylin V10 operating system. A QT-based interface is adopted to support human–machine interaction during the experiments. Data exchange between the shore-based and onboard systems is achieved through a wireless communication radio. Control commands generated by the industrial computer are transmitted to a PLC controller, which further drives the rudder servo and throttle servo through analog output signals, thereby enabling accurate execution of steering and propulsion commands.

Due to the limited availability of experimental vessels, moving obstacles are represented by virtual target ships (TSs) in the experimental program. The mathematical model of the virtual obstacles follows (44), where $n = 1, \ldots, 3$ denotes the index of the target ship. Specifically, the initial positions, velocities, and motion starting times of the three TSs are given as :$(x^1_{\text{init}}, y^1_{\text{init}}) = (-144, -120)$, $(v^1_{\text{obs},x}, v^1_{\text{obs},y}) = (-0.3, 0)$, $t^1_{\text{start}} = 83$; $(x^2_{\text{init}}, y^2_{\text{init}}) = (-275, -121)$, $(v^2_{\text{obs},x}, v^2_{\text{obs},y}) = (0.6, -0.6)$, $t^2_{\text{start}} = 167$; and $(x^3_{\text{init}}, y^3_{\text{init}}) = (-292.34, -273.16)$, $(v^3_{\text{obs},x}, v^3_{\text{obs},y}) = (0.28, 0.96)$, $t^3_{\text{start}} = 240$, respectively.

Fig. 14 presents the simulation-based validation results constructed from historical trajectory data collected during real USV experiments. Specifically, Fig. 14(a) illustrates the trajectory tracking and dynamic obstacle-avoidance maneuvers of the unmanned surface vehicle (USV) in the presence of three virtual target ships (TS1–TS3). In this complex encounter scenario, TS1, TS2, and TS3 emulate three representative encounter situations, namely **overtaking**, **crossing**, and **head-on**, respectively. The trajectory results demonstrate that the USV is capable of accurately identifying different encounter situations and executing appropriate avoidance maneuvers in compliance with the COLREGs collision-avoidance rules when facing target threats from various directions.

Fig. 14(b) depicts the evolution of the relative distances between the USV and each target ship. It can be observed that, throughout the entire navigation process, the relative distances between the own ship and all obstacles are strictly maintained above the predefined safety threshold of 10 m, thereby validating the safety performance of the proposed algorithm. Fig. 14(c) shows the real-time tracking performance of the actual heading angle with respect to the desired heading command, indicating that the control system achieves fast dynamic response and high-precision tracking. Fig. 14(d) illustrates the evolution of the position errors between the USV coordinates and the smoothed reference trajectory. Under the action of the proposed dynamic virtual guidance system (DVGS), the USV is able to converge smoothly and rapidly toward the reference path. Even after temporary deviations caused by obstacle-avoidance maneuvers, the system can promptly and stably guide the USV to re-capture the reference trajectory once the risk region is cleared.

Figure 15 illustrates the real-time navigation trajectories of the USV recorded during maritime field trials alongside aerial snapshots captured by a UAV. Figure 15.a presents the real-time USV trajectory captured via the electronic nautical chart monitoring interface, superimposed with the motion paths of virtual Target Ships (TSs) to intuitively demonstrate the complete obstacle avoidance maneuver. Specifically, Figure 15.a(I) shows the global trajectory reconstructed in MATLAB using historical longitude and latitude data, while Figure 15.a(II) provides a sequence of UAV aerial snapshots at an 8 s sampling interval, capturing the actual pose variations of the USV during the avoidance process. As a localized magnified view, Figure 15.b displays the fusion of real-world aerial snapshots and virtual TS trajectories, clearly observing that the USV accurately executes rule-compliant maneuvers driven by the virtual obstacles. These experimental results not only verify the robustness of the proposed algorithm under real sea conditions but also further demonstrate the practical implementability and engineering value of the proposed scheme in physical systems.

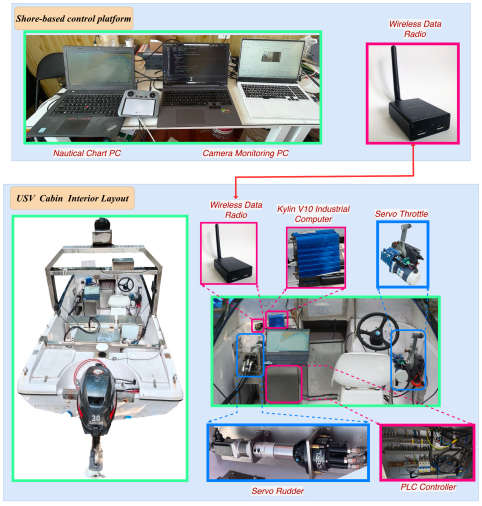


Fig. 13 System architecture of the USV experimental verification platform.

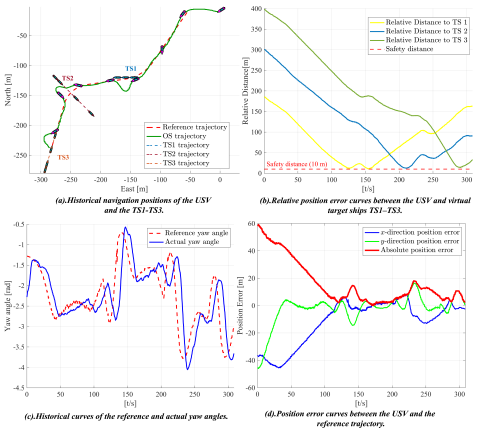


Fig. 14 Position and yaw angle curves plotted based on historical navigation data.

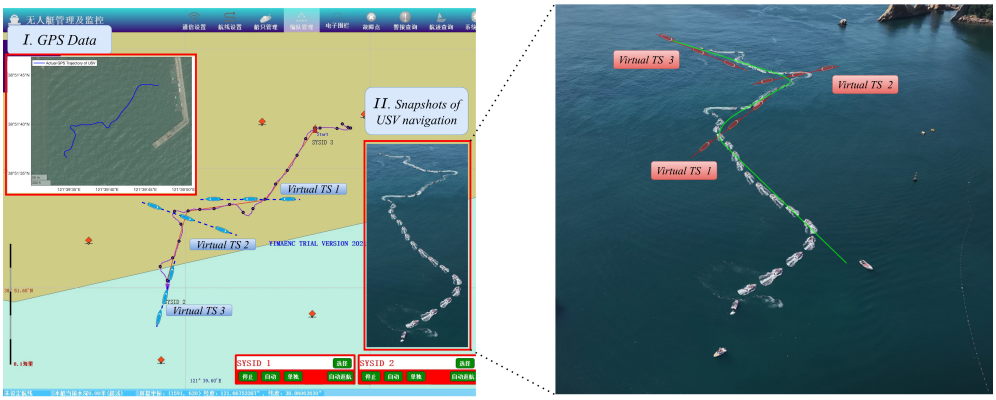


Fig. 15 Nautical chart showing the trajectory together with the overhead USV navigation trajectory captured by a UAV.

5 Conclusions

This paper proposes a safety control strategy for USV waypoint-following missions under target obstacle vessels and unknown external disturbances, aiming at practical deployment in marine engineering. First, a VOBCG-based obstacle avoidance planner is developed to satisfy COLREGs constraints while maintaining trajectory continuity, thereby avoiding the trajectory oscillations often observed in conventional VO-based methods. Its effectiveness and practicability are validated through sea trials. Second,

an FT-FO controller is designed to observe external disturbances and guarantee fixed-time stability for USV navigation under disturbances. It should be noted that the FT-FO controller has not yet been validated in sea trials; instead, a T-S fuzzy controller was used in the experiments. This is mainly because a complete USV dynamic model was initially required, but the low-cost thrusters used on the platform did not provide rotational-speed data, making such modeling difficult. Future work will incorporate rotational-speed feedback to improve the USV dynamic model, based on which the FT-FO controller will be experimentally validated. Event-triggered and fault-tolerant control mechanisms will also be investigated to further enhance system robustness and engineering applicability in complex marine environments.

Declarations

Competing interests

The authors declare that the research was conducted in the absence of any commercial or financial relationships that could be construed as a potential conflict of interest.

Funding

This work was supported by National Natural Science Foundation of China (Grant number 52301360),Liaoning Province Natural Science Foundation (Grant number 2025-MSLH-081), Liaoning Provincial Science and Technology Plan Joint (Grant number 2025JH2/101800165), National Basic Research Program Project (Key technologies of three-party game in USV clusters),Dalian City Science and Technology Plan (Key) Project (Grant number 2024JB11PT007).

References

[1] Wang, Z., Zhao, Y., Mu, D., Sun, X., Wang, Y.: Fixed-time fuzzy formation control for underactuated surface vehicles based on a novel trajectory-guiding strategy under model uncertainties. Ocean Engineering **327**, 120715 (2025)

[2] Wang, Z., Zhao, Y., Mu, D., Liang, X., Wang, Y., Wang, Q.: Global fixed-time singularity-avoidance cooperative formation control of underactuated unmanned surface vehicles via waypoints guidance: Theory and experiment. Ocean Engineering **342**, 122552 (2025)

[3] Wang, Z., Zhao, Y., Mu, D., Wang, Z., Ma, Y., Wang, Y., Wang, Q.: Waypoints tracking for usvs employing fixed-time prescribed performance fuzzy inverse optimal control with marine experiment. ISA Transactions (2026)

[4] Dong, Z., Lu, S., Hu, Z., Liu, W., Ding, Y., Liu, Y.: Simultaneous modeling and backstepping control algorithm for trajectory tracking of underactuated usv based on real-time sailing data in complex ocean conditions. ISA transactions (2025)

[5] Hu, X., Wang, Y., Xu, J., Zhao, J., Xiao, B.: Dynamic output feedback fuzzy sliding mode learning attitude control for hypersonic flight vehicle with actuator rate constraint. Journal of the Franklin Institute, 108374 (2025)

[6] Bai, M., Sun, W.: Disturbance-resilient model predictive control for active suspension systems with perception errors in road preview information. Journal of the Franklin Institute, 107957 (2025)

[7] Yin, M., Zhao, Y., Li, F., Liu, B., Yang, C., Gui, W.: Collision avoidance control for limited perception unmanned surface vehicle swarm based on proximal policy optimization. Journal of the Franklin Institute **361**(6), 106709 (2024)

[8] Xiao, L., Liu, Y., Zuo, Q., Cao, M., Kuang, W.: A fuzzy weighted self-allocation sliding mode controller for uav trajectory tracking. Journal of the Franklin Institute, 108418 (2026)

[9] Tong, H., Sun, M., Luan, T., Xu, D.: Constrained control using novel nonlinear mapping for underactuated unmanned surface vehicles with unknown sideslip angle. ISA transactions **141**, 261–275 (2023)

[10] Huang, X., Liu, H., Tian, X., Yuan, J.: Guiding vector field and self-structuring learning network-based formation control of underactuated surface vessels in static obstacle environments with flexible performances. ISA transactions **153**, 96–116 (2024)

[11] Du, X., Yuan, X., Yang, B., Zhao, X.: Event-triggered trajectory tracking control for unmanned surface vessels with prescribed performance using barrier lyapunov functions. IEEE Transactions on Fuzzy Systems (2025)

[12] Zhang, X., Xu, X., Li, J., Zhang, Z., Zhang, Z., Brunauer, G.: Observer-based fuzzy adaptive fault-tolerant control for nsc system of usv with sideslip angle and steering machine fault. IEEE Transactions on Intelligent Vehicles **9**(1), 372–382 (2023)

[13] Xu, X., Zhang, X., Zhang, Z., Ma, F., Guan, C., Steyskal, F.: Los guidance for fuzzy adaptive fault-tolerant path following control of usv with side-slip compensation and actuator fault. IEEE Transactions on Transportation Electrification (2024)

[14] Lv, G., Peng, Z., Li, Y., Liu, L., Wang, D.: Barrier-certified model predictive cooperative path following control of connected autonomous surface vehicles. IEEE Transactions on Network Science and Engineering **10**(6), 3354–3367 (2023)

[15] Wen, G., Lam, J., Fu, J., Wang, S.: Distributed mpc-based robust collision avoidance formation navigation of constrained multiple usvs. IEEE Transactions on Intelligent Vehicles **9**(1), 1804–1816 (2023)

[16] Pan, R., Zhang, W., Wang, S., Kang, S.: Deep reinforcement learning model for multi-ship collision avoidance decision making design implementation and performance analysis. Scientific Reports **15**(1), 21250 (2025)

[17] Wang, Z., Chen, P., Chen, L., Mou, J.: Collaborative collision avoidance approach for usvs based on multi-agent deep reinforcement learning. IEEE Transactions on Intelligent Transportation Systems (2025)

[18] Fan, X., Kong, F., Xie, X., Guo, Y.: Enhanced dynamic window approach for autonomous obstacle avoidance in unmanned underwater vehicles. Scientific Reports (2026)

[19] Haraldsen, A., Wiig, M.S., Pettersen, K.Y.: A theoretical analysis of the velocity obstacle method for nonholonomic vehicles and underactuated surface vessels. IEEE Transactions on Control Systems Technology **32**(5), 1801–1816 (2024)

[20] Huang, J., Zeng, J., Chi, X., Sreenath, K., Liu, Z., Su, H.: Dynamic collision avoidance using velocity obstacle-based control barrier functions. IEEE Transactions on Control Systems Technology (2025)

[21] Han, R., Chen, S., Wang, S., Zhang, Z., Gao, R., Hao, Q., Pan, J.: Reinforcement learned distributed multi-robot navigation with reciprocal velocity obstacle shaped rewards. IEEE Robotics and Automation Letters **7**(3), 5896–5903 (2022)

[22] Gu, N., Wang, D., Peng, Z., Liu, L.: Observer-based finite-time control for distributed path maneuvering of underactuated unmanned surface vehicles with collision avoidance and connectivity preservation. IEEE Transactions on Systems, Man, and Cybernetics: Systems **51**(8), 5105–5115 (2019)

[23] Pan, Z., Zhang, C., Xia, Y., Xiong, H., Shao, X.: An improved artificial potential field method for path planning and formation control of the multi-uav systems. IEEE Transactions on Circuits and Systems II: Express Briefs **69**(3), 1129–1133 (2021)

[24] Zhang, G., Han, J., Li, J., Zhang, X.: Apf-based intelligent navigation approach for usv in presence of mixed potential directions: Guidance and control design. Ocean Engineering **260**, 111972 (2022)

[25] Li, J., Zhang, G., Liu, C., Zhang, W.: Colregs-constrained adaptive fuzzy event-triggered control for underactuated surface vessels with the actuator failures. IEEE Transactions on Fuzzy Systems **29**(12), 3822–3832 (2020)

[26] Lyu, H., Yin, Y.: Colregs-constrained real-time path planning for autonomous ships using modified artificial potential fields. The Journal of navigation **72**(3), 588–608 (2019)

[27] Wenming, W., Jialu, D., Yihan, T.: A dynamic collision avoidance solution scheme

of unmanned surface vessels based on proactive velocity obstacle and set-based guidance. Ocean Engineering **248**, 110794 (2022)

[28] Gonzalez-Garcia, A., Castañeda, H., De León-Morales, J.: Unmanned surface vehicle robust tracking control using an adaptive super-twisting controller. Control Engineering Practice **149**, 105985 (2024)

[29] Gong, X., Liu, L., Peng, Z., Wang, D., Zhang, W.: Resource-aware synchronized path following of multiple unmanned surface vehicles with experiments: A cooperative vector field approach. Control engineering practice **124**, 105184 (2022)

[30] Dong, Z., Hu, Z., Hou, J., Lu, S., Ding, Y., Liu, W., Liu, Y.: Parameter identification and real-time motion prediction for a water-jet unmanned surface vehicle based on online sparse least squares support vector machine algorithm. Control Engineering Practice **164**, 106508 (2025)

[31] Gonzalez-Garcia, A., Barragan-Alcantar, D., Collado-Gonzalez, I., Garrido, L.: Adaptive dynamic programming and deep reinforcement learning for the control of an unmanned surface vehicle: Experimental results. Control Engineering Practice **111**, 104807 (2021)

[32] Lv, M., Gu, N., Wang, D., Peng, Z.: Gvf-based guidance and super-twisting control of autonomous surface vehicle for target tracking in obstacle environments with experiments. Control Engineering Practice **133**, 105434 (2023)

[33] Zhang, H., Li, B., Xiao, B., Yang, Y., Ling, J.: Nonsingular recursive-structure sliding mode control for high-order nonlinear systems and an application in a wheeled mobile robot. ISA transactions **130**, 553–564 (2022)

[34] Cui, G., Zhuang, G., Lu, J.: Neural-network-based distributed adaptive synchronization for nonlinear multi-agent systems in pure-feedback form. Neurocomputing **218**, 234–241 (2016)

[35] Wang, H., Su, B.: Event-triggered formation control of auvs with fixed-time rbf disturbance observer. Applied Ocean Research **112**, 102638 (2021)

Supplementary Files

This is a list of supplementary files associated with this preprint. Click to download.

- 10xDJI.mp4